Antral Variation of Murine Gastric Pacemaker Cells Informed by Confocal Imaging and Machine Learning Methods

Sue Ann Mah, Recep Avci, Peng Du, Jean-Marie Vanderwinden, Leo K. Cheng

Abstract— The Interstitial Cells of Cajal (ICC) are specialized gastrointestinal (GI) pacemaker cells that generate and actively propagate electrophysiological events called slow waves. Slow waves regulate the GI motility necessary for digestion. Several functional GI motility disorders have been associated with depletion in the ICC. In this study, a validated Fast Random Forest (FRF) classification method using Trainable WEKA Segmentation for segmenting the networks of ICC was applied to confocal microscopy images of a whole mount tissue from the distal antrum of a mouse stomach ($583 \times 3,376 \times 133$ μm^3, parcellated into 24 equal image stacks). The FRF model performance was compared to 6 manually segmented subfields and produced an area under the receiver-operating characteristic (AUROC) of 0.95. Structural variations of ICC network in the longitudinal muscle (ICC-LM) and myenteric plexus (ICC-MP) were quantified. The average volume of ICC-MP was significantly higher than ICC-LM at any point throughout the antral tissue sampled. There was a pronounced decline of up to 80% in ICC-LM (from 3,705 μm^3 to 716 μm^3) over a distance of 279.3 μm, that eventually diminished towards the distal antrum. However, an inverse relationship was observed in ICC-MP with an overall increase of up to 157% (from 59,100 μm^3 to 151,830 μm^3) over a distance of approximately 2 mm that proceeds towards the distal antrum.

Clinical Relevance—Mapping the regional variations of ICC networks will provide insights into the relationship between ICC distribution, slow waves, and resultant gut motility. This will improve techniques for the diagnosis and treatment of functional GI motility disorders

I. INTRODUCTION

Interstitial Cells of Cajal (ICC) are specialized pacemaker cells that aid in the coordination of motility in the gastrointestinal (GI) tract through the generation of electrophysiological events termed slow waves (SWs) as well as a mediator of neuro-hormonal signals [1]. Loss of ICC, both in terms of structural degradation and pathophysiology, has been elucidated as a key disease mechanism in several pervasive clinical conditions, including gastroparesis, chronic unexplained nausea and vomiting, and Hirschsprung's disease [2]. Furthermore, loss of ICC is also associated with aging, at a rate of approximately 13% per every decade of life [3], which may translate to an increased burden of GI disorders in aging societies.

ICC form web-like network structures throughout the GI tract with several classes of ICC identified based on their anatomical locations in the GI wall. There are three layers of rhythmically active ICC networks that are electrically interconnected within the stomach wall of the murine antrum. A dense layer of ICC is situated within the myenteric plexus (ICC-MP) sandwiched between the longitudinal and circular muscle layers of the GI wall, with subsequent protrusions of the connected ICC-MP network into the intramuscular spaces of the longitudinal muscle layer (ICC-LM) and circumferential muscle layer (ICC-CM) [4].

Functionally, ICC mediate the propagation of SWs through a process called entrainment, where a syncytium of oscillators with different intrinsic frequencies converge to a single frequency with sustained phase-lags between the SWs generated by each ICC [5]. The ICC with lower intrinsic frequencies are entrained by neighboring ICC with higher intrinsic frequencies [6]. In the human stomach, gastric SWs are generally entrained to a single frequency of around 3 cycles per minute (cpm) and propagate in the antegrade towards the pyloric sphincter [1].

The present study utilizes a transgenic mouse model, enabling confocal imaging of full-thickness mouse gastric tissues [7]. A previously validated machine learning classifier [8] was employed to automatically segment ICC networks from the images. The segmented networks were then quantified for variations in terms of volume and thickness of ICC layer in the transmural direction with the aim of elucidating the ICC network transition in the distal stomach. Ultimately, this will facilitate a better understanding of the mechanisms underpinning the antrum/pyloric sphincter, and the diseases associated with its dysfunction, such as delayed gastric emptying [9].

II. METHODS

A. Experimental Images

Experimental methods were approved by the Université Libre de Bruxelles Animal Welfare Committee. A whole-mount tissue sample was obtained from a transgenic mouse stomach expressing enhanced green fluorescent proteins in the c-Kit positive ICC [7]. A longitudinal image tile with a volume of $583 \times 3,376 \times 133 \ \mu m^3$ from the distal stomach was acquired using a multiphoton microscope (LSM780NLO, Zeiss, Iena, Germany). The image tile was composed of 2×12 image stacks with 8% overlap, each with a volume of $304 \times 304 \times 133 \ \mu m^3$ (Fig. 1(a-c)), and a spatial resolution

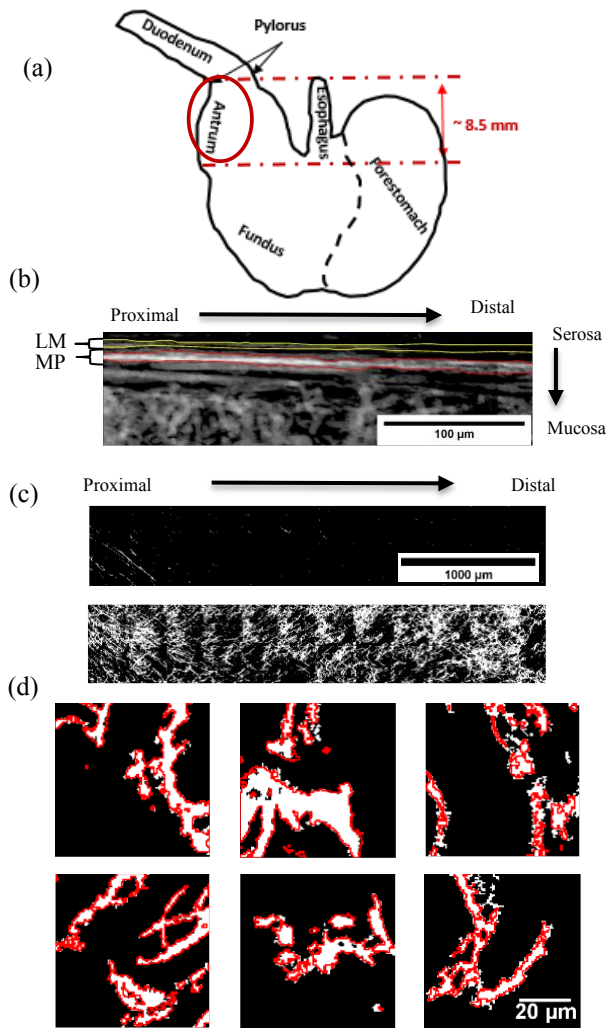of 0.59 μm in the imaging plane and 1 μm in the transmural direction.

Fig. 1. Confocal imaging data from mouse antrum. Shown are: (a) schematic and approximate location (red circle) where the confocal image tile was obtained, (b) cross sectional-projection of a segmented confocal volume block based on standard deviation of pixels. The longitudinal muscle (LM) layer (outlined in yellow) and myenteric plexus layer (MP) (outlined in red), (c) z-projection of all ICC over the region of the longitudinal muscle (LM) layer (top), and myenteric plexus layer (MP) (bottom), (d) the 6 randomly selected image subfields used to quantify the performance of the FRF model. The FRF model segmentations are outlined in red.

B. Machine Learning Segmentation

A previously validated machine learning model for segmenting ICC was implemented using the Trainable WEKA Segmentation plug-in in ImageJ [10]. Given the similarity to the type of data and accuracy of the previous validation step [8], the same Fast Random Forest (FRF) classifier was applied to the present dataset without further training.

A total of six subfields of $59 \times 59 \ \mu m^2$ were randomly selected from each image stack at equal distance along the longitudinal direction to serve as validation of the performance of segmentation (Fig. 1(d)). Each subfield was manually labeled, and the performance of the FRF classifier was evaluated by comparing the segmentation results with the manually labeled datasets [8]. The true positive rate and false positive rate across these 6 different decision thresholds were used to plot the receiver operating characteristic (ROC) curve. Then, 8 performance measures, namely Dice Coefficient, Jaccard Coefficient, Rand Index, Sensitivity, Specificity, Precision, Accuracy, and F-measure were computed to evaluate the performance of the FRF model.

Dice Coefficient is twice the overlapping area between ICC pixels in the manually segmented image and pixels identified by the classifier, divided by the total number of pixels in both images. Jaccard Coefficient is defined as the ratio of intersection between ICC pixels in the manually segmented image and pixels identified by the classifier, divided by its union. Sensitivity is the ratio between true positive (TP) pixels (i.e., the correctly identified ICC pixels by the classifier) and the total number of ICC pixels in the manually segmented image. As opposed to Sensitivity, Specificity measures the proportion of true negative (TN) pixels, non-ICC pixels that are correctly identified by the classifier. Rand Index may be viewed as a measure of the percentage of correct decisions made by the classifier. Precision is the ratio between TP pixels and total number of identified ICC pixels by the classifier. Accuracy is the proportion of TP pixels relative to the total number of the pixel in the image. F-measure is the harmonic mean between precision and recall for each image slice.

C. Manual Identification of Transmural ICC Network Types.

Following segmentation, each transmural slice (serosa to mucosa) was visually inspected to categorize image slices that belongs to the longitudinal muscle (LM) or the myenteric plexus (MP) region (Fig. 1 (b)) based on the networks of ICC-LM and ICC-MP that could be observed. Networks of ICC-LM were identified as the ICC close to the serosal surface with striated patterns following the LM fiber direction. Networks of ICC-MP were identified by its dense, bidirectional network following the LM layer.

D. ICC Network Quantification.

Following segmentation of the ICC networks using the FRF classifier, the ICC density (ρ_{ICC}) was computed for every slice in each image stack along the transmural direction (serosa to mucosa) and was found by taking the ratio of the number of pixels representing ICC over the total number of pixels in the image [8].

Our previously developed method [8] was applied to define the boundaries of the MP region for analysis of ICC-MP. For each confocal block, the slice with the highest ICC density ($\rho_{ICC,max}$) was identified and subsequently the lower (a) and upper (b) transmural image slices corresponding to a density of $0.5\rho_{ICC,max}$ were identified [8]. The total volume (μm^3) of ICC-MP that lies between the transmural slice from a to b in each confocal block were computed taking the sum of the total number of voxels segmented by the FRF classifier multiplied by the voxel volume. Next, the network layer thickness in μm was determined as follows,

$$Thickness = b - a + 1 \qquad (1)$$

Since ICC-LM is very sparse and not detected in most stacks, the boundaries of the LM region for analysis of ICC-LM were determined manually as described in Section II.C.

F. Analysis of Data

Data are expressed as mean ± standard deviation. Two-sample t-test was used where appropriate to evaluate differences in the data. P-values of less than 0.05 were considered statistically significant. The data were evaluated for n=24 confocal image stacks that make up the longitudinal antral image tile.

III. RESULTS

A. Performance of FRF Machine Learning Model

The ROC curve as shown in Fig. 2(a) with the resultant area under the receiver operating characteristic (AUROC) found to be 0.95, indicating an excellent performance. In addition, the average performance of the binary classifier was further evaluated for its Dice Coefficient (83±11%), Jaccard Coefficient (72±15%), Rand Index (95±2%), Sensitivity (75±17%), Specificity (99±1 %), Precision (95±3%), Accuracy (72 ±15 %) and F-measure (83 ±11%).
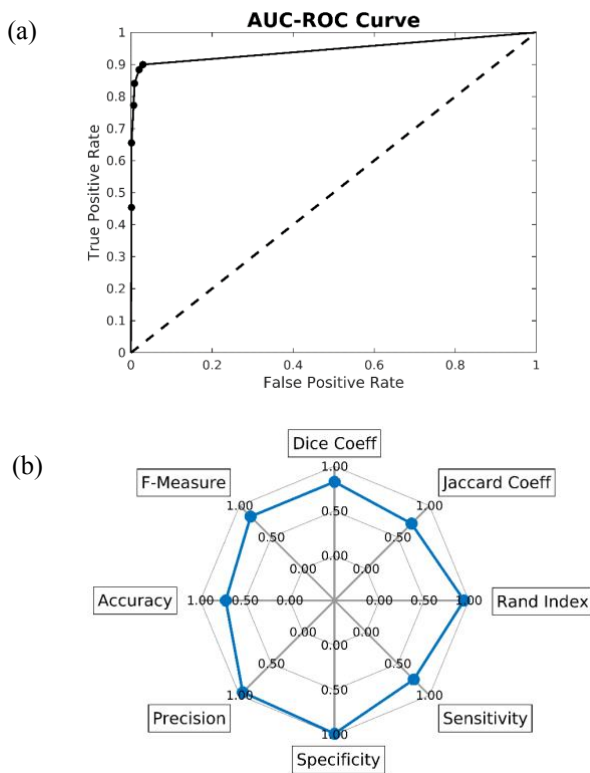

Fig 2. Performance of the FRF model. (a) The ROC curve for predicting ICC networks in a 2D image slice throughout the confocal images of the distal gastric tissue strip. (AUROC = 0.95). (b) Spider chart depicting evaluation based on 8 performance measures.

B. ICC-LM & ICC-MP spatial distribution

Figure 3(a) reveals pronounced decline longitudinally in the ICC-LM network volume within the LM layer from proximal to distal antrum. ICC-LM declined from 3,705 μm^3 to 716 μm^3 (80.7%) over a distance of 279.3 μm in the distal direction (i.e., from the 2nd to 3rd data point in Fig. 3(a)). Comparatively, ICC-MP increased in volume as it proceeds towards the distal antrum from 59,100 μm^3 to 151,830 μm^3 (156.9 %) over a distance of approximately 2 mm in the distal direction, as shown in Fig. 3(b). The average volume of ICC-MP was also higher than the average volume of ICC-LM (92,791 ± 35,649 μm^3 vs 869 ± 1,552 μm^3; p-value<0.001).
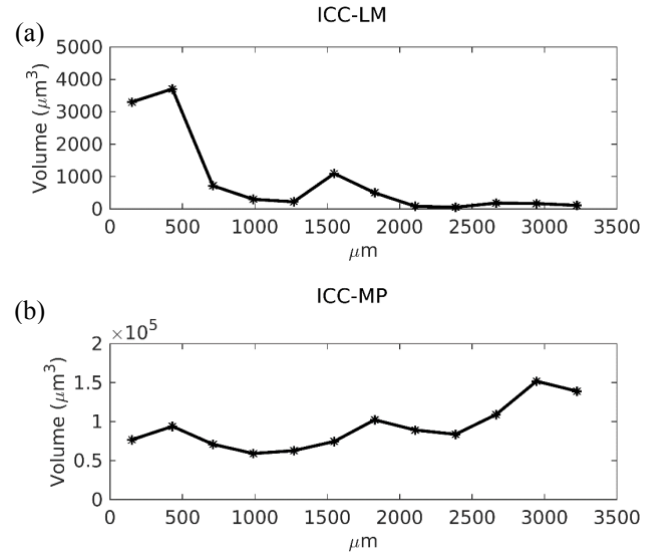

Figure 3: The network volume (μm^3) distribution of (a) ICC-LM and (b) ICC-MP across the imaged antral tissue strip.

The average thickness of the LM layer was 8.4 ± 3.3 μm and the average thickness of the MP layer was 15.4 ± 4.9 μm. There was a noticeable increase in the thickness of the MP layer from the average thickness of 14 μm to 22.5 μm at approximately 710 μm in the distal direction of the antrum, as shown in Fig. 4(b).
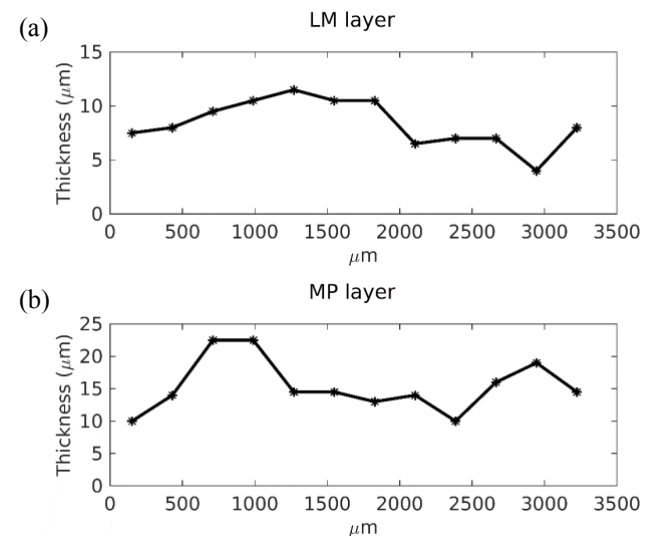

Figure 4: The distribution of the (a) LM layer and (b) MP layer thickness (μm) across the longitudinal antral image tile.

IV. DISCUSSION

We have extended our ongoing investigation [8] for the automated segmentation of ICC network from 3D confocal

tissue images of the mouse gastric antrum using the WEKA FRF technique. The spatial distributions of the segmented ICC-LM and ICC-MP networks throughout the longitudinal antral image tile were investigated in this paper. There were considerable variations observed in ICC-LM and ICC-MP network volume within the respective LM and MP layers of the murine antrum wall imaged.

The thickness of the LM layer was found to be approximately 4.0–11.5 μm thick; consistent with 5–10 μm thick LM layer as documented by Song et al. in the mouse antrum [11]. Furthermore, the marked deficiency in the network of ICC-LM observed in the gastric antrum were consistent with the previous observations [11], [12]. Cousins et al. [12] demonstrated sparse ICC-LM in the guinea-pig antrum, while Song et al. [11] reported complete absence of ICC-LM in the mouse antrum at a distance of 4 mm from the corpus-antrum border. ICC-LM are mainly present in the fundus and corpus, with the highest density along the greater curvature in the fundus and corpus [11]. This was further verified from our observation that ICC-LM network was only detected in the image stacks located nearest to the greater curvature at the corpus-antrum border (Fig. 1(c)). Thus, our results are agreeable to experimental observations made by Song et al. [11], and reinforce the present understanding that the density of ICC-LM significantly decreases from the proximal corpus to the antrum which eventually completely diminishes. Functionally, the diminished ICC-LM towards the pyloric sphincter would restrict the motility of the digesta in the aboral direction, which acts as a simple gate to control the outflow of chyme into the duodenum.

The ICC-MP form a dense and heterogeneous [13]–[15] network that lies in the myenteric region of the stomach wall. The network of ICC-MP spreads over the corpus and antrum with varying densities [16]. The overall increase in ICC-MP network volume from proximal to distal antrum as shown in Fig. 3(b) was consistent with the concept that SWs track towards the pylorus with increasing amplitude [17]–[19]. Previous imaging studies have also demonstrated a "break" in the ICC-MP in the gastroduodenal junction [20], which serves to isolate the gastric slow wave (3 cpm) from the intestinal slow waves (>10 cpm). While the techniques developed in here would be useful in tracking the gastroduodenal ICC break in future studies, a larger sample size is needed to validate the physiological insights of the spatial variations of ICC.

V. Conclusions

Structural variations of ICC were quantified in the distal mouse antrum. Elucidating the regional variations of ICC networks would allow a better understanding of the mechanisms underpinning the contractile patterns in the stomach and the diseases associated with its dysfunction.

References

[1] D. F. van Helden, D. R. Laver, J. Holdsworth, and M. S. Imtiaz, "Generation and propagation of gastric slow waves," *Clin. Exp. Pharmacol. Physiol.*, vol. 37, no. 4, pp. 516–524, Apr. 2010.

[2] S. A. Mah, R. Avci, L. K. Cheng, and P. Du, "Current applications of mathematical models of the interstitial cells of Cajal in the gastrointestinal tract," *Wiley Interdiscip. Rev. Syst. Biol. Med.*, p. e1507, Oct. 2020.

[3] P. J. Gomez-Pinilla *et al.*, "Changes in interstitial cells of cajal with age in the human stomach and colon," *Neurogastroenterol. Motil.*, vol. 23, no. 1, pp. 36–44, Jan. 2011.

[4] H. T. Lee *et al.*, "Septal Interstitial Cells of Cajal Conduct Pacemaker Activity to Excite Muscle Bundles in Human Jejunum," *Gastroenterology*, vol. 133, no. 3, pp. 907–917, 2007.

[5] L. K. Cheng, P. Du, and G. O'Grady, "Mapping and modeling gastrointestinal bioelectricity: from engineering bench to bedside.," *Physiology (Bethesda).*, vol. 28, no. 5, pp. 310–7, Sep. 2013.

[6] E. E. Daniel, B. L. Bardakjian, J. D. Huizinga, and N. E. Diamant, "Relaxation oscillator and core conductor models are needed for understanding of GI electrical activities.," *Am. J. Physiol.*, vol. 266, no. 3 Pt 1, pp. G339-49, Mar. 1994.

[7] S. Klein *et al.*, "Interstitial cells of Cajal integrate excitatory and inhibitory neurotransmission with intestinal slow-wave activity," *Nat. Commun.*, vol. 4, no. 1, p. 1630, Jun. 2013.

[8] S. A. Mah, R. Avci, P. Du, J.-M. Vanderwinden, and L. K. Cheng, "Supervised Machine Learning Segmentation and Quantification of Gastric Pacemaker Cells*," in *2020 42nd Annual International Conference of the IEEE Engineering in Medicine & Biology Society (EMBC)*, 2020, vol. 2020-July, pp. 1408–1411.

[9] J.-M. Vanderwinden, H. Liu, R. Menu, J.-L. Conreur, M.-H. De Laet, and J.-J. Vanderhaeghen, "The pathology of infantile hypertrophic pyloric stenosis after healing," *J. Pediatr. Surg.*, vol. 31, no. 11, pp. 1530–1534, Nov. 1996.

[10] M. Hall, E. Frank, G. Holmes, B. Pfahringer, P. Reutemann, and I. H. Witten, "The WEKA data mining software," *ACM SIGKDD Explor. Newsl.*, vol. 11, no. 1, p. 10, Nov. 2009.

[11] G. Song, G. David, S. Hirst, K. M. Sanders, and S. M. Ward, "Regional variation in ICC distribution, pacemaking activity and neural responses in the longitudinal muscle of the murine stomach," *J. Physiol.*, vol. 564, no. 2, pp. 523–540, Apr. 2005.

[12] H. M. Cousins, F. R. Edwards, H. Hickey, C. E. Hill, and G. D. S. Hirst, "Electrical coupling between the myenteric interstitial cells of Cajal and adjacent muscle layers in the guinea-pig gastric antrum," *J. Physiol.*, vol. 550, no. 3, pp. 829–844, Aug. 2003.

[13] A. J. Burns, A. E. J. Lomax, S. Torihashi, K. M. Sanders, and S. M. Ward, "Interstitial cells of Cajal mediate inhibitory neurotransmission in the stomach," *Proc. Natl. Acad. Sci. U. S. A.*, vol. 93, no. 21, pp. 12008–12013, Oct. 1996.

[14] G. D. S. Hirst, E. A. H. Beckett, K. M. Sanders, and S. M. Ward, "Regional variation in contribution of myenteric and intramuscular interstitial cells of Cajal to generation of slow waves in mouse gastric antrum," *J. Physiol.*, vol. 540, no. 3, pp. 1003–1012, May 2002.

[15] E. A. H. Beckett, C. A. McGeough, K. M. Sanders, and S. M. Ward, "Pacing of interstitial cells of Cajal in the murine gastric antrum: Neurally mediated and direct stimulation," *J. Physiol.*, vol. 553, no. 2, pp. 545–559, Dec. 2003.

[16] G. D. S. Hirst and F. R. Edwards, "Electrical events underlying organized myogenic contractions of the guinea pig stomach," *J. Physiol.*, vol. 576, no. 3, pp. 659–665, Nov. 2006.

[17] W. J. E. P. Lammers, L. Ver Donck, B. Stephen, D. Smets, and J. A. J. Schuurkes, "Origin and propagation of the slow wave in the canine stomach: the outlines of a gastric conduction system," *Am. J. Physiol. Liver Physiol.*, vol. 296, no. 6, pp. G1200–G1210, Jun. 2009.

[18] G. O'Grady *et al.*, "Origin and propagation of human gastric slow-wave activity defined by high-resolution mapping.," *Am. J. Physiol. Gastrointest. Liver Physiol.*, vol. 299, no. 3, pp. G585-92, Sep. 2010.

[19] R. Berry *et al.*, "Functional physiology of the human terminal antrum defined by highresolution electrical mapping and computational modeling," *Am. J. Physiol. - Gastrointest. Liver Physiol.*, vol. 311, no. 5, pp. G895–G902, 2016.

[20] X. Y. Wang, L. W. C. Liu, N. E. Diamant, and J. D. Huizinga, "Unique distribution of interstitial cells of Cajal in the feline pylorus," *Cell Tissue Res.*, vol. 329, no. 1, pp. 13–24, Jul. 2007.